This is the Author's [*accepted*] manuscript version of the following contribution:

[Ludovica Casnedi, Roberta Licheri, Michele Brun, Giorgio Pia, From nature geometry to material design: Advanced fractal nature analysis for predicting experimental elastic properties, Ceramics International, 46, 15, 15 October 2020, pagg. 23947-23955]

The publisher's version is available at:

When citing, please refer to the published version.

1

From nature geometry to material design:
Advanced fractal nature analysis for predicting experimental elastic properties

Ludovica Casnedi, Roberta Licheri, Michele Brun, Giorgio Pia[*]

Dipartimento di Ingegneria Meccanica, Chimica e dei Materiali, Università degli Studi di Cagliari, Piazza d'Armi, 09123 Cagliari, Italy.

* Corresponding author: Giorgio Pia, giorgio.pia@dimcm.unica.it, telephone +390706755051, fax +390706755067

Abstract

In this work, combined experimental and fractal nature analysis procedures are proposed in order to both model and design mechanical properties of porous ceramics. Several porous ceramics samples have been considered both from an in-situ experimental campaign and from the literature. Microstructural information concerning pore size distribution has been approximated by the Intermingled Fractal units (IFU) approach and effective mechanical properties are derived by a simple discrete model. The capability of the proposed methodology to reproduce high-scattered mechanical properties is fully shown and a comparison with classical bounds and estimates is also reported. Finally, the combined experimental, fractal nature analysis and homogenisation scheme is implemented as a design procedure for the technological production of advanced porous ceramics.

2

1. Introduction

Porous ceramics (*PCs*) represent a fundamental class of materials with diverse applications in numerous industrial, mechanical, chemical, environmental and civil engineering and architecture fields as filters, absorbers, fuel cell electrodes, hot gas collectors, engine components, biomaterials applications, piezo-electric materials and thermal and acoustical insulators. Their extensive employment is owing to low weight [1,2], fractional density [3] and heat conduction [4] coupled with an excellent surface abrasion and strain resistance, considerable hardness mechanical strength and chemical inertness [5–8].

Many different fabrication methods can be applied to produce these materials [9,10]: gelcasting process [11,12], organic foam technique [13], freeze casting method [14–16] and pore-forming agent (PFA) method [4,17]. The PFA method consists of: (i) preparing samples of clay powders and PFA by using compaction or extrusion techniques; (ii) sintering specimens, where the PFA is burnt out forming a porous microstructure during this thermal treatment. The formation of porosity into ceramics microstructure is a complicate process conditioned by several variables such as granulometry and composition of powders which comprise of raw materials, ball milling process for decreasing powders dimension and mixing them creating relative heterogeneity, different methods for shaping objects, variation of environmental condition for moisture and drying speed (temperature, thermal gradient) [18,19]. The variation of these aspects can generate microstructure modifications in pore morphology as shape, tortuous length, dimension and size distribution. Consequently, *PCs* microstructures change remarkably. Indeed, thermal conduction, liquid or vapour-gas transfer and mechanical response are a result of the existence and relative characteristics of voids in the microstructures.

The possibility to pre-determine the performances by a material design is the real target of Materials Science. It is really challenging to have an excellent balance between different performances. An example is the relationship between heat transfer and mechanical behaviour. Indeed, heat conduction and mechanical stiffness tend to decrease when porosity increases. This effect must be evaluated especially for the fabrication of structural-insulating materials. Moreover, when porosity increases, transport phenomena are remarkable and decay processes related to water presence in pore structure can be strongly accelerated. On the contrary, building materials characterised by low porosity prevent the water vapour permeability, which may be negative for indoor comfort [20,21].

In this sense, a sensible improvement is gained from the control of microstructural variables and final characteristics of materials in terms of efficiency, reliability and an appropriate longer service life. The capability of determining structural morphology *a priori* is an aspiration issue for improving mechanical performances. They depend on several aspects such as elastic and plastic behaviour, the

3

existence of pores and the morphology of microstructure [22–24]. Different equations help in describing mechanical response by using density or porosity values and empirical parameters, but they cannot give precise bounds in the case of porous media (see the lower Reuss[25] and the upper Voigt[26] bounds). The Hashin-Shtrikman bounds[27,28] are known to give the closest possible bounds depending only on the porosity and explicit expressions are given for particulate composites. Anyway, it is well-known that the lower bounds in porous composites reduce to zero.

Higher-order microstructural information, such as microstructural disorder and pore size distribution (*psd*) influence the effective behaviour [29–31]. Recently, the attempts inspired by fractal geometry, have displayed to be promising for describing porous microstructures. Fractal geometry was first formalised by Mandelbrot in 1970s. Starting from empirical observations it is possible to observe that "mountains are not cones, clouds are not spheres, and surfaces are not smooth" [32]. Consequently, Euclidean geometry is insufficient for describing natural shapes, while fractal geometry is capable to represent their complexity. For this, fractal geometry has been used in different areas ranging from social science to computer technology, economics and materials science [32]. Fractal figures can be elaborated easily by an iterative procedure, which consists of the proposition of the same mapping rules reproduced at different scales and they are suitable to represent complex schemes comparable to multidisperse natural or artificial shapes. The recurring pattern, usually defined as self-similarity, leads to simplified analytical algorithms thanks to the implementation of repetitive equations. Therefore, fractal geometries can be implemented to describe morphological information such as *psd* by means of an analytical recursive algorithm and they are appropriate to model multidisperse complex microstructures.

Relevant applications of fractal geometry have been shown. Cai et al. [33–36] considered porous characteristics (sizes, shape and tortuosity) to study liquid and gas circulation in different materials, Yu et al. [37] proposed an equation with fractal parameters to compute permeability, diffusivity and thermal conductivity of porous cement pastes, Qin et al. [38] formalised a theoretical fractal nature analysis to explain thermal and fluid transfer in unsaturated and saturated porous media and Liang et al. [39] estimated the effective diffusivity of electrolyte in porous media. In these works, calculations based on fractal geometry showed a remarkable agreement with experimental data.

In the last years, a systematic study on the effect of porous microstructure on macroscopic properties and consequent performances has been conducted by adopting the Intermingled Fractal units' model (IFU). Its capability of reproducing *psd* and pore fraction p is important for the prediction of physical quantities such as thermal and energy transport behaviour [40–47].

Here, the IFU procedure is first applied in order to determine macroscopic mechanical properties of different classes of *PCs*. Several comparisons are performed from experimental data obtained both

4

from the literature and from an experimental campaign developed in the present work. The approach is briefly described and a comparison with classical bounds is also included. The capability of the IFU approach to fit experimental macroscopic stiffness values, including the effect of polydispersity, is fully shown. Moreover, a final simulation paves the way of a combined procedure for fabricating *PCs* with specific mechanical properties; in this procedure pre-design predictions from IFU and simple experimental data can be used in order to develop a technology for the large scale production of *PCs* with targeted macroscopic mechanical properties.

2. Materials and methods

Five sets of *PCs* are considered, fabricated with different procedures. The first series (*A*), fabricated by Novais et al.[4], has been manufactured by mixing and sintering clay powders: (*a*) with particles size smaller than 250 μm, (samples *A1-4*); (*b*) with powder particle size in the range of 250-425 μm (samples *A5-8*), plus polypropylene ICORENE PP CO14RM as PFA; (*c*) with particles size smaller than 250 μm (samples *A9-12*) and (*d*) with powder particle size in the range of 250-425 μm (samples *A13-16*), plus polymethyl methacrylate VSE UVT PMMA as PFAs.

Porosity estimation has been performed by using the Mercury Intrusion Porosimetry (MIP) technique [4]. Elastic behaviour has been estimated by three-point bending strength measurements performed by Shimadzu Auto-graph AG 25TA. The experimental set up for displacement speed is 0.5 mm min^{-1}.

The second series (*B*) has been realised by De Bonis et al. [48]. A first system (*B-IS*) has been produced with clays from the Island of Ischia (*B-IS*). Clays are initially kept in water for some hours in order to achieve a semi-liquid consistency. Successively, 10% of volcanic beach sand, extracted from Campi Flegrei, is added in the mixture *B-IS*.

A second system (*B-SO*) has been fabricated by using clays from Sorrento, Italy. Eight specimens with dimensions 120 mm × 80 mm × 40 mm were produced. Raw bricks were dried for 10 days under controlled environmental conditions (T=25°C, HR=50%) and put under a fire in an electric muffle furnace. Two heating rates were used; from environment temperature to 200°C, 1.5°C/min, and from 200 °C to the maximum *T*, 3°C/min. The soaking time was 90 min, while the cooling was carried out in accordance with the free drift of the switched off kiln.

Seven samples, fired at 700, 800, 850, 900, 950, 1000 and 1100°C, are tested for each system of ceramics (*B-IS* and *B-SO*); they are labelled as *B-ISi* and *B-SOi* (*i*=1,…,7). *Psd* was obtained experimentally from MIP and elastic moduli from ultrasound tests.

The third series (*C*) of ceramics was produced by Màrquez et al. [49] from kaolinitic clay, feldspar and quartz sand. Powders preparation is performed by planetary ball-milling technique. The final

5

mixture was dried in an oven at 110°C, sieved to pass at 150 μm and then pressed at 40 MPa in order to realise two types of samples: (*a*) cylindrical samples with a diameter (ϕ) of 20 mm and a height of 5 mm and (*b*) tiles of dimension 50 mm × 50 mm × 8 mm. Seven samples were produced, sintered at 1200, 1230, 1250, 1260, 1270, 1280 and 1300°C. The samples are labelled as *Ci* (*i*=1,…,7). The measurement of open porosity and bulk density has been done following ASTM C373-88 and ASTM C329-88. Elastic moduli where determined from the resonance frequency method (Grindosonic analyser).

The fourth series (D*i*, *i*=1,…,9) has been taken by Gültekin [50]. They prepared nine samples of porcelain tile granules with the uniaxial pressing procedure at 450 kgf/cm^2 in a rectangular formwork (50 mm × 100 mm). *D1-3* were sintered at 1210°C, *D4-6* at 1220 °C and *D7-9* at 1230°C. Sintering rates were 40, 50, 60 °C/min, respectively, while cooling rate was 60°C/min, common for all the samples. The open porosity was measured using the Archimedes method. Indirect method based on ultrasonic propagation was used to obtain elastic moduli.

The fifth series of samples (*E*), were produced at the Advanced Materials Lab of the Department of Mechanical, Chemical and Material Engineering of the University of Cagliari. They were fabricated starting from commercial green clays (20 g per sample), ball milled with sodium chloride (NaCl) in different volume concentrations (from 0 up to 55 vol.%) for 20 minutes. Ball milling has been performed inside a polyethylene jar by using zirconia balls with a diameter equal to 5 mm and total mass of 4 g. Firing procedure and consolidation were obtained by Spark Plasma Sintering (SPS) apparatus (515S model, Fuji Electronic Industrial Co., Ltd., Kanagawa, Japan)[46]. Briefly, this equipment is based on the combination of a uniaxial press (max 50 kN) with a DC pulsed current generator (10 V, 1500 A, 300 Hz), to simultaneously provide an electric current through the sample and the graphite die containing it, together with a mechanical load through the die punches. Specifically, NaCl-clay mixtures were first cold compacted inside a graphite die (30 mm outside diameter; 15 mm inside diameter; 30 mm height) and then sintered at 780°C (heating rate of 100°C/min) for about 10 min, under a mechanical pressure of 20 MPa and vacuum conditions. Cylindrical samples of about 14.7 mm diameter and 4 mm height are obtained. NaCl has been subsequently removed by dissolution in hot distilled water. Sample density, measured after NaCl removal, is between 1.26 g/cm^3 and 2.09 g/cm^3. More details on SPS procedure is reported Licheri et al.[51] In Table 1 we report the bulk density ρ, the porosity p, the sintering temperature T and the experimental elastic modulus (E_{exp}) for different *A*, *B*, *C*, *D* systems [4,48–50]. Bulk density varies between 1.76 and 3.69 g/cm^3. Comparing *PCs* series, elastic stiffnesses are very different. Indeed, E_{exp} is between 0.91 and 65 GPa.

Elastic modulus of the solid phase is E_s = 6.8 GPa for Novais samples A, E_s = 20 GPa for De Bonis samples B and E_s = 76 GPa for Màrquez and Gültekin samples C [52,53].

3. Intermingled Fractal Units' (IFU) model

IFU model has been designed for simulating porous microstructure characteristics and, in particular, *psd* of materials. The phenomenological method for building this fractal nature analysis is grounded in using Sierpinski carpet as a tale unit. Every fractal, the Sierpinski carpet, has been obtained by an iterative process in which a defined construction mapping rule is repeated at different scales. Specifically, in this case, the procedure starts from dividing the sides of a square by factor (F), which is here equal to 3. Consequently, 9 sub-squares are generated (Fig. 1). At each iteration i, some of the 9 sub-squares are removed. The resulting figure comprises of voids and solid squares (s). The scheme is repeated generating a recursive image with fractal dimension

$$D_f = \frac{\log(s)}{\log(F)}. \tag{1}$$

Iteration by iteration, a void microstructure and consequent *psd* are generated. For real porous structures, the iterations are calibrated on the pore size range (*psr*), measured by MIP. However, a single Sierpinski carpet cannot model every *psd,* since the associated pore size R vs cumulative porosity curves have constant curvature (as a consequence of the fact that the cumulative porosity is a geometric series normalised to one). This fact limits the possibility to model the *psd* of several *PCs*. To overcome this restriction the IFU model has been proposed in [52,54]; it is based on the combination of two different Sierpinski carpets, labelled α and β. This set of intermingled fractal figures gives rise to a new porous system, which could have a non-fractal configuration and allows reproducing experimental data acquired by MIP tests. The number n_β of β base units is combined per single α tale is

$$n_\beta = \frac{(A_{\alpha p} - p \cdot A_\alpha)}{(p \cdot A_\beta - A_{\beta p})}, \tag{2}$$

where A_α, A_β and $A_{\alpha p}$, $A_{\beta p}$ represent total surfaces and total pore surfaces of units α and β, respectively [42].

In order to fit the total porosity of the *PCs* samples (obtained by SPS, Fig. 2a), at each iteration *solid forever* tiles (solid sub-squares) are used and a solid phase, namely *filled surface*, is also added at the larger scale into the model [43], see Fig. 2b. This expedient increases the versatility of reproducing pore volume distribution, Fig. 2c. In this way, IFU represents a cross sectional area of the minimum representative part of material. The input data of the model, experimentally acquired by MIP tests, are the maximum ray of the *psr* (the ray corresponding to a variation in Hg absorption) and the porous

7

volume fraction as a function of the pore size. This has a notable importance for the generalisation of the model which, indeed, can be used for different porous materials [44,54]. By changing Sierpinski characteristics, it is possible to determine the porosity and, subsequently, the *psd,* which fits the experimental MIP data. Therefore, these steps are useful for replicating experimental microstructures (Fig. 2c), predicting their elastic behaviour (Fig. 2d) and design new porous microstructures (Fig. 2e) with specific mechanical properties (Fig. 2f).

These fractal patterns are constructed and the IFU parameters are reported in Tables 2, 3 and 4 for different samples' data. They contains fractal dimension, D_f of Sierpinski carpets α and β, which defines the geometric configuration of the fractal unit; the size of larger pore ray, R_{max}; the size of smaller pore ray, R_{min}; the iterations that determine the *psr*; number of *solid forever* squares contained in Sierpinski carpet and *filled surface*.

The application of IFU procedure allows reproducing pore cumulative curves for different *PCs*. In Fig. 3 we show the results for *PCs* by De Bonis [48]. The excellent agreement between experimental and numerical curves demonstrates the capability and the versatility of the advanced fractal nature analysis to reproduce pore cumulative distribution. Indeed, it gives the possibility to include effects of polydispersion, obtained from experimental data, into the homogenisation scheme.

From the defined microstructure an analytical multiscale homogenisation scheme is implemented. Every unit is converted into a spring pattern (Fig. 2d) and, at each iteration *i*, the effective Young's modulus $E^{(i)}$ is computed by means of a simple scheme made of springs in series and parallel. A recursive bottom-up algorithm is implemented from the smaller to the larger cells. At last iteration *n* (the smallest cell for a Sierpinski carpet), the stiffness of each spring associated to a single sub-square is estimated as

$$k_{qr}^{(n)} = \chi_{qr} \, E_s \, \frac{A_e^{(n)}}{L_e^{(n)}}, \qquad q = I, II, III, \qquad r = 1, 2, 3, \tag{3}$$

where E_s is the Young's modulus of the solid phase, $A_e^{(n)}$ the cross-sectional area (per unit out-of-plane thickness) and $L_e^{(n)}$ the length of the corresponding sub-square. The characteristic function χ_{qr} is equal to 1 for solid sub-squares and 0 for void ones. Following the simple spring pattern connected in parallel and series indicated in Fig. 2d, the effective spring stiffness for the 3×3 unit cell is

$$k^{(n)} = \left[\sum_{q=I,II,III} \left(\frac{1}{\sum_{r=1,2,3} k_{qr}^{(n)}} \right) \right]^{-1}. \tag{4}$$

The derivation of equation (4) is reported in the Supplementary material.

Since $A_e^{(n)}$ and $L_e^{(n)}$ are the same in all sub-squares the effective Young's modulus is given by

$$E^{(n)} = \left[\sum_{q=I,II,III} \left(\frac{1}{\sum_{r=1,2,3} E_{qr}^{(n)}} \right) \right]^{-1}, \tag{5}$$

where $E_{qr}^{(n)} = \chi_{qr} E_s$.

As an example, for the cell of Fig. 1

$$E^{(n)} = \frac{3}{4} E_s . \tag{6}$$

At the next iterations

$$E^{(i)} = \left[\sum_{q=I,II,III} \left(\frac{1}{\sum_{r=1,2,3} E_{qr}^{(i)}} \right) \right]^{-1}, \qquad i = n-1, n-2, \dots, 1, \tag{7}$$

where $E_{qr}^{(i)}$ is equal to 0 for a void sub-square, $E^{(i+1)}$ for a carpet sub-square and E_s for a *solid forever* sub-square.

At larger scale, the Sierpinski carpets α and β are complemented by the solid *filled surface*.

The harmonic average of Young's modulus of each base units (Sierpinski carpets α and β) and *filled surface* (having modulus E_s) corresponds to the final E_{IFU}.

4. Analytical estimates

Several analytical models have been proposed to estimate or bound the Young's modulus as a function of microstructural information. In the following, we report bounds and estimates, which depends on the porosity p, namely the one-point correlation function of the microstructure.

The upper Hashin-Shtrikman (E_{HS}) bound [27,28] for particulate composites reads as

$$E_{HS} \le E_s \frac{1-p}{1+p} \tag{8}$$

and the derivation of the simplified formula is reported in the Supplementary material. The corresponding lower bound reduces to zero.

The Voigt expression (E_V) [26,55,56] is the arithmetic average

$$E_V \le E_s(1-p), \tag{9}$$

which is an upper bounds; the corresponding lower bound is the Reuss harmonic average, which reduces again to zero.

The exponential relation (E_{exp}) [57] has the form

$$E_{exp} = E_s exp\left(\frac{-2p}{1-p} \right) \tag{10}$$

and the simplified expression of Gibson and Ashby (E_{GA}) is[58]

$$E_{GA} = E_s\{[\phi^2(1-p)^2] + [(1-\phi)(1-p)]\} . \tag{11}$$

9

The Gibson and Ashby estimate (11) considers open and closed cells in foams (see Chapter 1.2 [58]), in addition to the porosity, ϕ is the solid fraction of the structural elements which defines the open cells. For foams, characterised by open cells, $\phi = 1$.

Finally, an empirical model is also reported [59]

$$E_R = E_s \left(1 - \frac{p}{p_0}\right)^n,$$ (12)

where, in the case of spherical pores (E_{R1}), $n = 1.65$ and $p_0 = 0.818$, for ellipsoidal pores (E_{R2}), $n = 2.25$ and $p_0 = 0.798$ and for solid spheres (E_{R3}), $n = 2.23$ and $p_0 = 0.652$.

Equations (8-12) give estimations and bounds of the Young's modulus based on the porosity, the first order statistical information regarding the microstructure. Some additional information are given by the open cell parameter ϕ in the Gibson and Ashby expression (11) and by the parameters n and p_0 associated to the pore shape.

5. Results

A comparison between experimental data and analytical estimates from the literature is reported in Fig. 4, where the normalised effective elastic modulus $E_{eff} = E/E_s$ is shown as a function of the porosity p. Estimates and bounds (8-12) are shown by dotted lines, while experimental moduli are indicated by points as follows: ▲ systems A (Novais [4]), ■ systems B-IS (De Bonis [48]), ● systems B-SO (De Bonis [48]), ▬ systems C (Màrquez [49]) and ◆ systems D (Gültekin [50]). Despite of the general trend of a decrease of the Young's modulus with the porosity p, indicated by the coloured region, it is evident that the experimental values display large oscillation. Although porosity certainly influences mechanical properties, it does not simply correlate to elastic behaviour in unequivocal way. The analytical models in equations (8-12), which depend only on the porosity, cannot track such high scattering. By observing experimental results reported in Fig. 4, we note that there is no monotonic dependence on the porosity p, as shown, in particular, by systems B-IS and C. Indeed, a deeper inspection of experimental results reveals that B-$IS6$ and B-$SO3$ have porosity $p \approx 0.38$, but their effective Young's modulus is equal to 0.49 and 0.06, respectively. This large variation takes place also for systems which are fabricated with the same methods: B-$IS1$ and B-$IS7$, with $p \approx 0.31$, have effective Young's modulus equal to 0.56 and 0.24, respectively, while $A4$, $A7$ and $A12$, with $p \approx 0.22$, have very scattered E_{eff}; equal to 0.29, 0.59 and 0.37, respectively. This data evidence, at least qualitatively, the role of the microstructure, its morphology, topology and solid phase disorder in determining the effective behaviour of PCs.

Equations (8-12) are representative for specific materials for which they are formalised, but, at the same time, they cannot be considered for making a generalised procedure for PCs. In order to achieve

10

a better approximation in predicting the elastic behaviour, different models that can incorporate the available experimental data, in particular *psd* from MIP tests, must be employed. Here, we show that approaches based on fractal geometry, named the Intermingled Fractal units' model (IFU) has the capability to predict with high precision the macroscopic behaviour of *PC*s.

Estimates of the Young's modulus provided by the IFU model are reported in Fig. 5. Experimental values are given in coloured points and estimates by white ones. Novais (triangles) [4] and De Bonis (squares and circles) [48] samples are considered. In part (a) of the figure the effective Young's modulus E_{eff} is given as a function of porosity, while a direct comparison between experimental values and IFU estimates is shown in part (b), where the 45% straight line indicates perfect agreement. It is fully evident the capability of the IFU model to fit experimental data. Despite of the coarse homogenization scheme based on the spring pattern model, the fractal geometry embeds the effect of polydispersion by reproducing, to a high level of precision, the *psd* in the experimental size interval. It turns out that this is a key microstructural parameter that influences, to a large extent, the macroscopic properties of the porous system.

The predictions calculated for these *PCs* demonstrate the highest versatility of IFU and they push to apply this procedure as a design tool for the production of materials realised with a specific porous microstructure and targeted elastic properties. In Fig. 6 we show the pore cumulative curves for different *PC*s. *E1* and *E2* systems (blue lines), fabricated at the Advanced Materials Lab by SPS techniques, have porosity p equal to 0.22 and 0.53, respectively and a *psd* characterised by two picks corresponding to pores with ray-size equal to 0.011 µm and 0.027 µm and 0.018 µm and 0.11 µm, respectively. The different microstructures depend on the amount of pore-forming agent (PFA) during the PCs production. Pore cumulative curves of systems *E1* and *E2* are compared with IFU modelling reconstruction *M1* and *M2* (red dotted lines), and, as before, they are in excellent agreement with experimental values. Moreover, in the same figure we report the pore cumulative curves predicted by the fractal natureanalyses of designed pore microstructures (*F1-F8*) computed by modulating the total porosity p. The IFU curves M1-2, F1-8 are obtained by setting up the IFU model with the parameters specified in Tables 3 and 4. The resulting combinations represent microstructures definition for *PCs* with specific elastic properties, which have to be calculated by fractal natural analysis.

Consequently, as seen before, Young's modulus is calculated by resolving series and parallel springs' patterns. These IFU calculation data are presented in Fig. 7 as a function of porosity. They fall down within the coloured area which represents the experimental trends by Novais, De Bonis, Màrquez and Gültekin [4,48–50] from Fig. 4, but they clearly incorporated statistical information of the microstructure beyond the porosity p.

Conclusion

The possibility to design porous ceramics represents a desired target for Materials Science researchers. It would provide the opportunity to predict materials behaviour in different conditions. In particular, it is very useful for the effective mechanical properties. Different analytical models have been published in literature, but they do not give precise estimates for the classes of porous ceramics considered in this work. The fractal nature analysis has the capability to represents the internal microstructure, which develops at different scales and naturally fits with the available microstructural experimental data, in particular the pore size distribution. Since it is associated with the internal geometry, it can be applied to the analysis of different physical fields and here it is implemented to the case of mechanical behaviour of PC. The IFU approach combines different fractal units and can reproduce the pore size distribution of the sample to a high level of precision. It is applied here for the first time to compute the macroscopic mechanical properties. In particular, Young's modulus has been calculated by considering the available microstructural data of the porous structure. The phenomenological reproduction is then converted into series and parallel patterns, analytically solved for calculating elastic modulus. IFU modelling has been estimated by comparing calculations with experimental data of Novais, De Bonis, Màrquez and Gültekin systems. The capability of the fractal nature analysis to reproduce the polydispersive nature of the microstructure is a key point that enables to retrieve high-scattered effective properties. For designed materials, the elaborations obtained by the application of IFU analytical equations predict effective Young's Modulus in very good agreement with data acquired experimentally.

Appendix 1. Determination of effective spring stiffness

The 3×3 cell is modelled as a system of springs where, in each row I, II, III the springs at columns 1, 2, 3 are connected in parallel and the three rows are then connected in series.

Then, the spring stiffness of each row k_q^n is obtained coupling in parallel the spring in each row, namely

$$k_q^{(n)} = \sum_{r=1,2,3} k_{qr}^{(n)} , \qquad q = I, II, III. \tag{A. 1.1}$$

The effective stiffness k^n of the cell is obtained coupling in series the row stiffnesses of equation (A. 1.1) as follows

$$\frac{1}{k^{(n)}} = \Sigma_{q=I,II,III} \frac{1}{k_q^{(n)}} \tag{A. 1.2}$$

leading to expression (4).

Appendix 2. Hashin-Shtrikman bounds

The Hashin-Shtrikman variational principle provide rigorous lower and upper bounds for the macroscopic constitutive properties of composites [27]. In the case of a well-ordered particulate two phase composite, which is linear elastic and macroscopically isotropic, explicit expressions are given for the effective shear μ and the compressibility K moduli.

Considering a two-phase heterogeneous material with volume fractions p_1 and $p_2 = 1 - p_1$ and elastic moduli $\mu_1 < \mu_2$ and $K_1 < K_2$, the bounds are as follows

$$K_- \leq K \leq K_+ \,, \tag{A. 2.1}$$

$$\mu_- \leq \mu \leq \mu_+ \,, \tag{A. 2.2}$$

where

$$\begin{cases} K_- = K_1 + \dfrac{p_2}{\frac{1}{K_2-K_1}+\frac{p_1}{K_1+\frac{4}{3}\mu_1}} \,, \\[4mm] K_+ = K_2 + \dfrac{p_1}{\frac{1}{K_1-K_2}+\frac{p_2}{K_2+\frac{4}{3}\mu_2}} \,, \end{cases} \tag{A. 2.3}$$

and

$$\begin{cases} \mu_- = \mu_1 + \dfrac{p_2}{\frac{1}{\mu_2-\mu_1}+\frac{6(K_1+2\mu_1)p_1}{5(3K_1+4\mu_1)\mu_1}} \,, \\[4mm] \mu_+ = \mu_2 + \dfrac{p_1}{\frac{1}{\mu_1-\mu_2}+\frac{6(K_2+2\mu_2)p_2}{5(3K_2+4\mu_2)\mu_2}} \,. \end{cases} \tag{A. 2.4}$$

For a porous composites $p_1 = p$, $p_2 = 1 - p$ (p is the porosity), $\mu_1 = K_1 = 0$ and $\mu_2 = \mu_s$, $K_2 = K_s$. In such a case, it is easy to check from (A. 2.3) and (A. 2.4) that the lower bounds μ_- and K_- reduce to zero.

Then, remembering that

$$E = \frac{9K\mu}{3K+\mu} = \frac{1}{\frac{1}{3\mu}+\frac{1}{9K}} \,, \tag{A. 2.5}$$

it is possible to construct bounds for the Young's modulus E from the bounds (A. 2.3) and (A. 2.4) as follows

$$E_- \leq E \leq E_+ \,, \tag{A. 2.6}$$

where $E_- = \left(\frac{1}{3\mu_-} + \frac{1}{9K_-}\right)^{-1}$ reduces to zero in the porous case, while

$$E_+ = \frac{1}{\frac{1}{3\mu_+}+\frac{1}{9K_+}} = \frac{2\,E_S(1-p)(7-5\nu_S)}{2(7-5\nu_S)+(13-2\nu_S-15\nu_S^2)p} \,, \tag{A. 2.7}$$

13

with ν_s the Poisson's coefficient of the solid phase.

Expression (A. 2.7) has a minimum at $\nu_s = \frac{7-4\sqrt{2}}{5} = 0.269$ and the difference between the minimum and the maximum value of E_+/E_s in the wide interval $0 \leq \nu_s \leq 0.5$ increases with p, being 0.43% for $p = 0.05$ and 4.12% for $p = 0.8$. It is therefore justified to consider $\nu_s = 0.2$ leading to the simplified expression

$$E_+ = E_s \frac{1-p}{1+p}, \tag{A. 2.8}$$

corresponding to the upper limit in equation (8).

References

[1]   S. Li, C.-A. Wang, J. Zhou, Effect of starch addition on microstructure and properties of highly porous alumina ceramics, Ceram. Int. 39 (2013) 8833–8839. doi:10.1016/j.ceramint.2013.04.072.

[2]   H. Xu, J. Liu, A. Guo, H. Du, Z. Hou, Porous silica ceramics with relatively high strength and novel bi-modal pore structure prepared by a TBA-based gel-casting method, Ceram. Int. 38 (2012) 1725–1729. doi:10.1016/j.ceramint.2011.09.013.

[3]   Z. Hou, J. Liu, H. Du, H. Xu, A. Guo, M. Wang, Preparation of porous Y2SiO5 ceramics with relatively high compressive strength and ultra-low thermal conductivity by a TBA-based gel-casting method, Ceram. Int. 39 (2013) 969–976. doi:10.1016/j.ceramint.2012.07.014.

[4]   R.M. Novais, M.P. Seabra, J. a. Labrincha, Ceramic tiles with controlled porosity and low thermal conductivity by using pore-forming agents, Ceram. Int. 40 (2014) 11637–11648. doi:10.1016/j.ceramint.2014.03.163.

[5]   A.S. Wagh, R.B. Poeppel, J.P. Singh, Open Pore Description of Mechanical-Properties of Ceramics, J. Mater. Sci. 26 (1991) 3862–3868.

[6]   S.. Baldacim, C. a. . Cairo, C.R.. Silva, Mechanical properties of ceramic composites, J. Mater. Process. Technol. 119 (2001) 273–276. doi:10.1016/S0924-0136(01)00931-1.

[7]   F. Rey-García, F. Gutiérrez-Mora, C.J. Borrel, L.C. Estepa, L.A. Angurel, G.F. De La Fuente, Microstructural characterization and tribological behavior of Laser Furnace processed ceramic tiles, Ceram. Int. 44 (2018) 6997–7005. doi:10.1016/j.ceramint.2018.01.133.

[8]   A. Andrés, M.C. Díaz, A. Coz, M.J. Abellán, J.R. Viguri, Physico-chemical characterisation

of bricks all through the manufacture process in relation to efflorescence salts, J. Eur. Ceram. Soc. 29 (2009) 1869–1877. doi:10.1016/j.jeurceramsoc.2008.11.015.

[9] G. Xu, Y. Ma, H. Cui, G. Ruan, Z. Zhang, H. Zhao, Preparation of porous mullite–corundum ceramics with controlled pore size using bioactive yeast as pore-forming agent, Mater. Lett. 116 (2014) 349–352. doi:10.1016/j.matlet.2013.11.067.

[10] E. Chevalier, D. Chulia, C. Pouget, Fabrication of Porous Substrates : A Review of Processes Using Pore Forming Agents in the Biomaterial Field, 97 (2008) 1135–1154. doi:10.1002/jps.

[11] Y. Liu, X. Liu, G. Li, G. Meng, Low cost porous mullite-corundum ceramics by gelcasting, 6 (2001) 3687–3692.

[12] W. Xue, Y. Huang, Z. Xie, W. Liu, Al 2 O 3 ceramics with well-oriented and hexagonally ordered pores : The formation of microstructures and the control of properties, 32 (2012) 3151–3159.

[13] J.-H. Ha, R. Ahmad, I.-H. Song, A novel method of coating a particle-stabilized alumina foam on a porous alumina substrate, Mater. Lett. 88 (2012) 40–42. doi:10.1016/j.matlet.2012.08.007.

[14] Y.-H. Koh, E.-J. Lee, B.-H. Yoon, J.-H. Song, H.-E. Kim, H.-W. Kim, Effect of Polystyrene Addition on Freeze Casting of Ceramic/Camphene Slurry for Ultra-High Porosity Ceramics with Aligned Pore Channels, J. Am. Ceram. Soc. 89 (2006) 3646–3653. doi:10.1111/j.1551-2916.2006.01311.x.

[15] Y. Tang, Q. Miao, S. Qiu, K. Zhao, L. Hu, Novel freeze-casting fabrication of aligned lamellar porous alumina with a centrosymmetric structure, J. Eur. Ceram. Soc. 34 (2014) 4077–4082. doi:10.1016/j.jeurceramsoc.2014.05.040.

[16] H.-L. Hu, Y.-P. Zeng, Y.-F. Xia, D.-X. Yao, K.-H. Zuo, High-strength porous Si3N4 ceramics prepared by freeze casting and silicon powder nitridation process, Mater. Lett. 133 (2014) 285–288. doi:10.1016/j.matlet.2014.06.176.

[17] H. Ge, G. Wang, B. Yuan, B. Dong, H. Li, Fabrication and microstructure of porous SiC ceramics using suspension emulsions as pore-forming agents, Ceram. Int. 40 (2014) 11705–11711. doi:10.1016/j.ceramint.2014.03.182.

[18] C. Coletti, G. Cultrone, L. Maritan, C. Mazzoli, Combined multi-analytical approach for study of pore system in bricks: How much porosity is there ?, Mater. Charact. 121 (2016) 82–92.

15

doi:10.1016/j.matchar.2016.09.024.

[19]   G. Cultrone, E. Sebastián, K. Elert, M.J. de la Torre, O. Cazalla, C. Rodriguez–Navarro, Influence of mineralogy and firing temperature on the porosity of bricks, J. Eur. Ceram. Soc. 24 (2004) 547–564. doi:10.1016/S0955-2219(03)00249-8.

[20]   J. Berger, S. Gasparin, D. Dutykh, N. Mendes, Accurate numerical simulation of moisture front in porous material, Build. Environ. 118 (2017) 211–224. doi:10.1016/j.buildenv.2017.03.016.

[21]   S. You, W. Li, T. Ye, F. Hu, W. Zheng, Study on moisture condensation on the interior surface of buildings in high humidity climate, Build. Environ. 125 (2017) 39–48. doi:10.1016/j.buildenv.2017.08.041.

[22]   A. Neves Junior, R.D. Toledo Filho, E. de Moraes Rego Fairbairn, J. Dweck, The effects of the early carbonation curing on the mechanical and porosity properties of high initial strength Portland cement pastes, Constr. Build. Mater. 77 (2015) 448–454. doi:10.1016/j.conbuildmat.2014.12.072.

[23]   J. Sun, Z. Hu, J. Li, H. Zhang, C. Sun, Thermal and mechanical properties of fibrous zirconia ceramics with ultra-high porosity, Ceram. Int. 40 (2014) 11787–11793. doi:10.1016/j.ceramint.2014.04.008.

[24]   X. Chen, S. Wu, J. Zhou, Influence of porosity on compressive and tensile strength of cement mortar, Constr. Build. Mater. 40 (2013) 869–874. doi:10.1016/j.conbuildmat.2012.11.072.

[25]   A. Reuss, Calculation of the flow limits of mixed crystals on the basis of the plasticity of the monocrystals, Z. Angew. Math. Mech. 9 (1929) 49–58.

[26]   W. Voigt, Ueber die Bezienhung zwischen den beiden Elasticitäts-constanten isotroper, Ann. Phys. 38 (1889) 573–587.

[27]   Z. Hashin, S. Shtrikman, On some variational principles in anisotropic and nonhomgeneous elasticity, J. Mech. Phys. Solids. 10 (1962) 335–342.

[28]   Z. Hashin, S. Shtrikman, A variational approach to the theory of the elastic behaviour of multiphase materials, J. Mech. Phys. Solids. 11 (1963) 127–140.

[29]   J. Zheng, Y. Ju, X. Zhao, Influence of pore structures on the mechanical behavior of low-permeability sandstones : numerical reconstruction and analysis, 1 (2014) 329–337. doi:10.1007/s40789-014-0020-7.

[30] H. Wang, Y. Liu, Y. Song, Y. Zhao, J. Zhao, D. Wang, Fractal analysis and its impact factors on pore structure of artificial cores based on the images obtained using magnetic resonance imaging, J. Appl. Geophys. 86 (2012) 70–81. doi:10.1016/j.jappgeo.2012.07.015.

[31] S.-C. Kou, C.-S. Poon, M. Etxeberria, Influence of recycled aggregates on long term mechanical properties and pore size distribution of concrete, Cem. Concr. Compos. 33 (2011) 286–291. doi:10.1016/j.cemconcomp.2010.10.003.

[32] B.B. Mandelbrot, The fractal geometry of nature, Freeman and Company, New York, 1982.

[33] J. Cai, B. Yu, M. Zou, L. Luo, Fractal Characterization of Spontaneous Co-current Imbibition in Porous Media, Energy & Fuels. 24 (2010) 1860–1867. doi:10.1021/ef901413p.

[34] J. Cai, B. Yu, A Discussion of the Effect of Tortuosity on the Capillary Imbibition in Porous Media, Transp. Porous Media. 89 (2011) 251–263. doi:10.1007/s11242-011-9767-0.

[35] J. Cai, X. Hu, D.C. Standnes, L. You, An analytical model for spontaneous imbibition in fractal porous media including gravity, Colloids Surfaces A Physicochem. Eng. Asp. 414 (2012) 228–233. doi:10.1016/j.colsurfa.2012.08.047.

[36] J. Cai, E. Perfect, C.-L. Cheng, X. Hu, Generalized Modeling of Spontaneous Imbibition Based on Hagen–Poiseuille Flow in Tortuous Capillaries with Variably Shaped Apertures, Langmuir. 30 (2014) 5142–5151. doi:10.1021/la5007204.

[37] P. Yu, Y.H. Duan, E. Chen, S.W. Tang, X.R. Wang, Microstructure-based fractal models for heat and mass transport properties of cement paste, Int. J. Heat Mass Transf. 126 (2018) 432–447. doi:10.1016/j.ijheatmasstransfer.2018.05.150.

[38] X. Qin, J. Cai, P. Xu, S. Dai, Q. Gan, A fractal model of effective thermal conductivity for porous media with various liquid saturation, Int. J. Heat Mass Transf. 128 (2019) 1149–1156. doi:10.1016/j.ijheatmasstransfer.2018.09.072.

[39] M. Liang, C. Fu, B. Xiao, L. Luo, Z. Wang, A fractal study for the effective electrolyte diffusion through charged porous media, Int. J. Heat Mass Transf. 137 (2019) 365–371. doi:10.1016/j.ijheatmasstransfer.2019.03.141.

[40] G. Pia, L. Casnedi, U. Sanna, Porous ceramic materials by pore-forming agent method: An intermingled fractal units analysis and procedure to predict thermal conductivity, Ceram. Int. 41 (2015) 6350–6357. doi:10.1016/j.ceramint.2015.01.069.

[41] G. Pia, High porous yttria-stabilized zirconia with aligned pore channels: Morphology

17

directionality influence on heat transfer, Ceram. Int. 42 (2016) 19–22. doi:10.1016/j.ceramint.2016.04.078.

[42] M. Brun, L. Casnedi, G. Pia, Bending strength of porous ceramics tiles : Bounds and estimates of e ff ective properties of an Intermingled Fractal Units ' model, Ceram. Int. 44 (2018) 10241–10248. doi:10.1016/j.ceramint.2018.03.028.

[43] G. Pia, M.L. Gualtieri, L. Casnedi, P. Meloni, F. Delogu, C. Siligardi, Microstructural evolution in porous ceramics subjected to freezing-thawing cycles: Modelling experimental outcomes, Ceram. Int. 44 (2018) 16992–16998. doi:10.1016/j.ceramint.2018.06.141.

[44] G. Pia, U. Sanna, A geometrical fractal model for the porosity and thermal conductivity of insulating concrete, Constr. Build. Mater. 44 (2013) 551–556. doi:10.1016/j.conbuildmat.2013.03.049.

[45] G. Pia, L. Casnedi, Heat transfer in high porous alumina: Experimental data interpretation by different modelling approaches, Ceram. Int. 43 (2017) 9184–9190. doi:10.1016/j.ceramint.2017.04.071.

[46] R. Licheri, L. Casnedi, B. Lasio, P. Meloni, G. Pia, Thermal behaviour of clay ceramics obtained by Spark Plasma Sintering: Is fractal geometry a new possible road to design porous structures?, Ceram. Int. 44 (2018) 21710–21716. doi:10.1016/j.ceramint.2018.08.259.

[47] G. Pia, L. Casnedi, R. Ricciu, L.A. Besalduch, O. Cocco, A. Murru, P. Meloni, U. Sanna, Thermal properties of porous stones in cultural heritage: Experimental findings and predictions using an intermingled fractal units model, Energy Build. 118 (2016) 232–239. doi:10.1016/j.enbuild.2016.03.011.

[48] A. De Bonis, G. Cultrone, C. Grifa, A. Langella, V. Morra, Clays from the Bay of Naples (Italy): New insight on ancient and traditional ceramics, J. Eur. Ceram. Soc. 34 (2014) 3229–3244. doi:10.1016/j.jeurceramsoc.2014.04.014.

[49] J. Martín-Márquez, J.M. Rincón, M. Romero, Effect of microstructure on mechanical properties of porcelain stoneware, J. Eur. Ceram. Soc. 30 (2010) 3063–3069. doi:10.1016/j.jeurceramsoc.2010.07.015.

[50] E. Eren Gültekin, The effect of heating rate and sintering temperature on the elastic modulus of porcelain tiles, Ultrasonics. 83 (2018) 120–125. doi:10.1016/j.ultras.2017.06.005.

[51] R. Licheri, C. Musa, R. Orrù, G. Cao, D. Sciti, Bulk monolithic zirconium and tantalum

18

diborides by reactive and non-reactive spark plasma sintering, J. Alloys Compd. 663 (2016) 351–359.

[52]   G. Pia, L. Casnedi, M. Ionta, U. Sanna, On the elastic deformation properties of porous ceramic materials obtained by pore-forming agent method, Ceram. Int. (2015). doi:10.1016/j.ceramint.2015.05.057.

[53]   D.N. Boccaccini, A.R. Boccaccini, Dependence of ultrasonic velocity on porosity and pore shape in sintered materials, J. Nondestruct. Eval. 16 (1997) 187–192. doi:10.1023/A:1021891813782.

[54]   C. Atzeni, G. Pia, U. Sanna, Fractal modelling of medium–high porosity SiC ceramics, J. Eur. Ceram. Soc. 28 (2008) 2809–2814. doi:10.1016/j.jeurceramsoc.2008.03.039.

[55]   W. Voigt, Lehrbuch der kristallphysik, Pranava Books, 1910, n.d.

[56]   A. Reuss, Berechnung der Fliehgrenze von Mischkristallen auf Grund der Plastizittitsbedingung fiir Einkristalle, Z. Angew. Math. Mech. 8 (1928) 49–58.

[57]   E. Rambaldi, W. Pabst, E. Gregorová, F. Prete, M.C. Bignozzi, Elastic properties of porous porcelain stoneware tiles, Ceram. Int. 43 (2017) 6919–6924. doi:10.1016/j.ceramint.2017.02.114.

[58]   L.J. Gibson, M.F. Ashby, Cellular Solids: Structure and Properties, 2nd ed., Cambridge University Press, 1997, Cambridge (UK), n.d.

[59]   A.P. Roberts, E.J. Garboczi, Elastic Properties of Model Porous Ceramics, J. Am. Ceram. Soc. 83 (2000) 3041–3048. doi:10.1111/j.1151-2916.2000.tb01680.x.

Captions

Figure 1. Sierpinski carpet. The geometrical construction starts from a square divided in 9 sub-squares. At each iteration i, 2 squares are removed generating the void microstructure. For i=1 voids have ray R_{max} (the characteristic size). Iteration by iteration, pore structure grows until the last iteration in which pores have ray $R_{min.}$ In the figure the fractal dimension is $D_f = \log(7)/\log(3) = 1.771$.

Figure 2. Experimental activity and modelling design by using IFU. (a) Sintering obtained by SPS; (b) *Filled surface* and *solid surface* for Sierpinski carpet with three pores at first iteration; (c) Hg intrusion tests and phenomenological IFU modelling; (d) elastic modulus calculations performed by using IFU equations; (e) porous microstructural design and elastic modulus estimations, (f) IFU calculations for designed microstructures are compared with experimental data.

Figure 3. Pore cumulative curves. Comparison between MIP data (continuous lines) and IFU modelling (dotted lines). Curves are given for *B-IS6* (a), *B-IS7* (b), *B-SO6* (c) and *B-SO7* (d) samples. IFU parameters are reported in Table 2.

Figure 4. Effective Young's modulus as a function of porosity p. Experimental data are indicated with points and analytical estimates by dotted-lines. ▲ Samples *A* (Novais [4], Es = 6.8 GPa), ■ samples *B-IS* (De Bonis [48], Es = 20 GPa), ● samples *B-SO* (De Bonis [48], Es = 20 GPa), ▬ samples *C* (Márquez [49], Es = 76 GPa) and ♦ samples *D* (Gültekin [50], Es = 76 GPa). Calculations are performed by using: Hashin-Shtrikman (HS), equation (8); Voigt (V), equation (9); exponential relation, (exp) equation (10); simplified expression of Gibson and Ashby, (GA) equation (11) and Roberts relations (R1-R3), equation (12). The coloured area shows the experimental trend of Young's modulus as a function of porosity.

Figure 5. Experimental data vs IFU estimations. Young's modulus is given for *PC*s by Novais (triangles) [4] and De Bonis (squares and circles) [48]. (a) Young's modulus as a function of porosity; coloured points correspond to experimental values, white points to IFU estimates. (b) Comparison between experimental data and IFU estimation.

20

Figure 6. Pore cumulative curves. *E1* and *E2* (blue lines): experimental value from MIP test. *M1* and *M2* (red dotted lines): reconstruction by fractal nature analysis. *F1-F8* (green dotted lines): prediction by fractal nature analysis.

Figure 7. Comparison between IFU data and experimental trends. Young's modulus calculations (●) are compared with experimental trends acquired by [4,48–50].
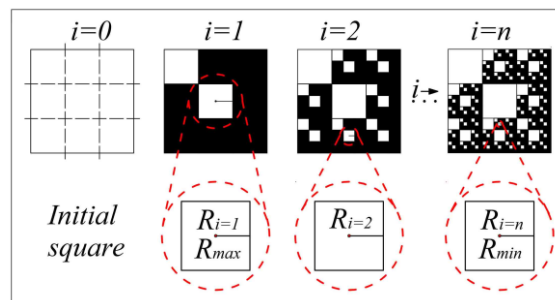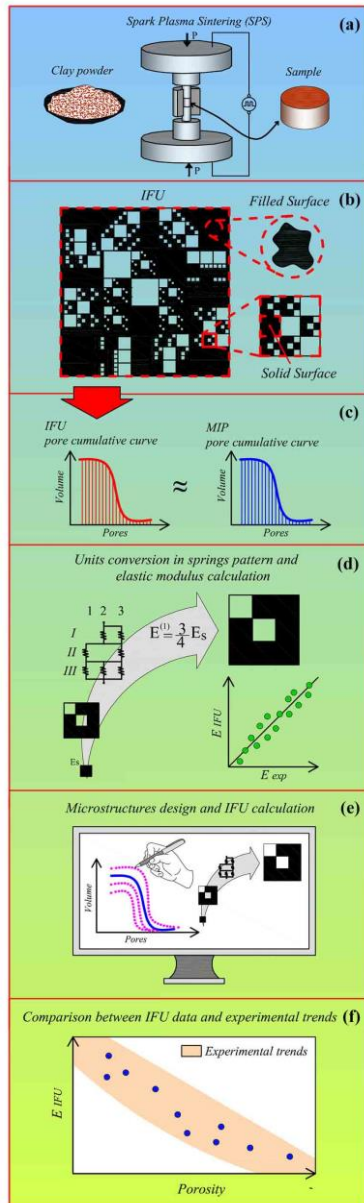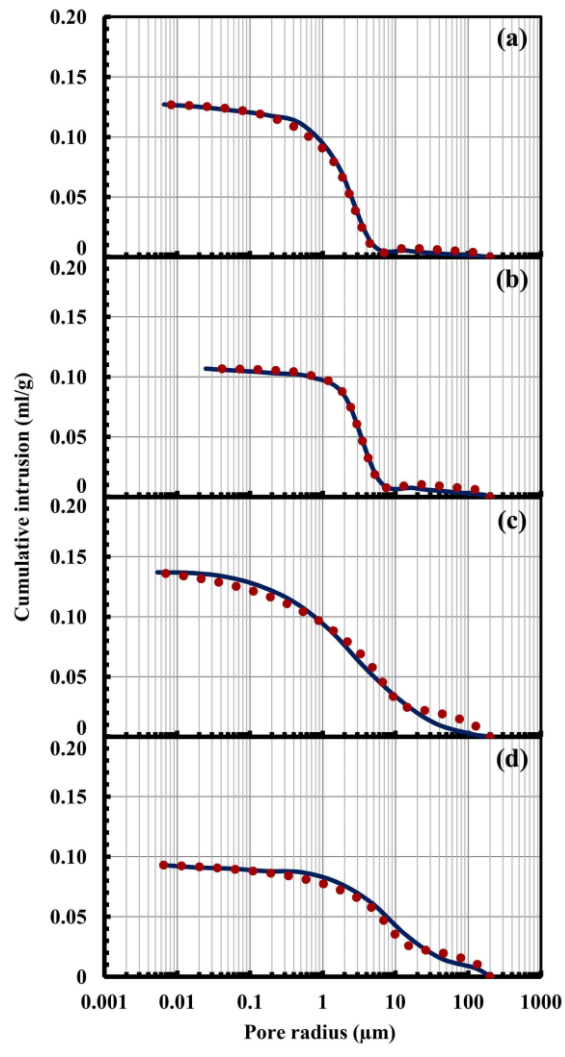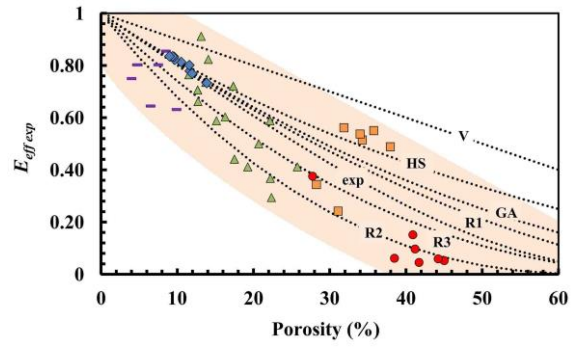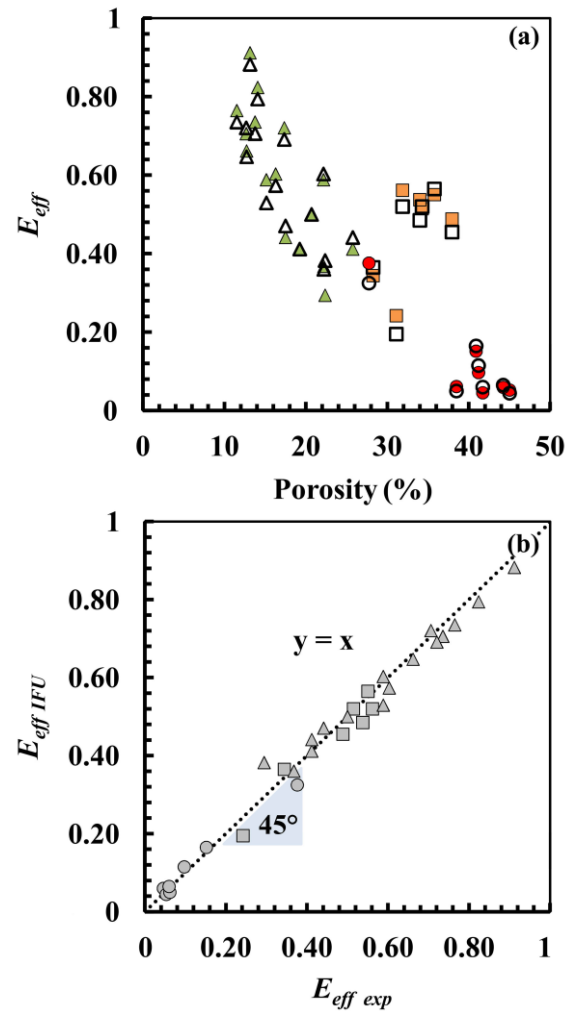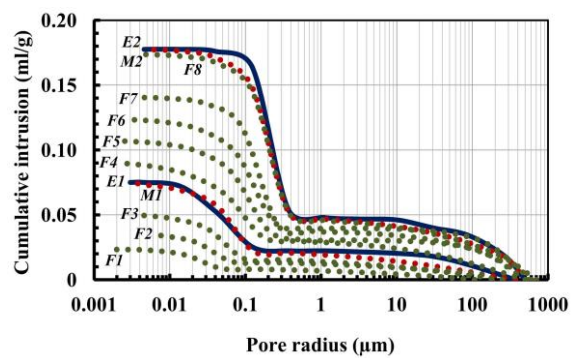

Fig. 1

Fig. 2

22

Fig.3
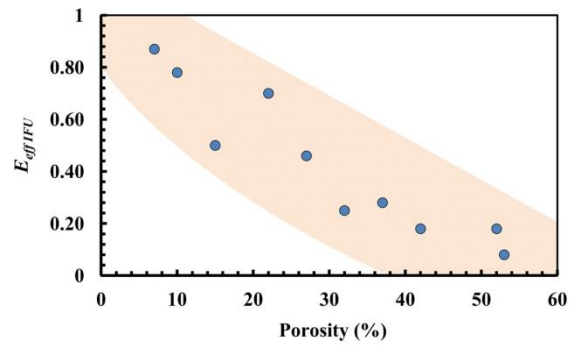
Fig. 4

Fig. 5

25

Fig. 6

Fig. 7

Table 1. Bulk density (ρ), porosity (p), sintering temperature (T) and experimental elastic modulus (E_{exp}) for A, B, C and D systems.

Sample	ρ (g/cm^3)	p (%)	T (°C)	E_{exp} (GPa)
A1	2.11	12.71	1200	4.5
A2	2.04	15.14	1200	4.0
A3	1.94	19.24	1200	2.8
A4	1.85	22.35	1200	2.0
A5	2.12	12.67	1200	4.8
A6	2.01	16.28	1200	4.1
A7	1.86	22.16	1200	4.0
A8	1.76	25.75	1200	2.8
A9	2.07	13.13	1200	6.2
A10	2.07	14.07	1200	5.6
A11	2.00	17.49	1200	3.0
A12	1.88	22.20	1200	2.5
A13	2.10	11.51	1200	5.2
A14	2.07	13.75	1200	5.0
A15	1.97	17.34	1200	4.9
A16	1.88	20.68	1200	3.4
B-IS1	2.45	31.09	700	4.84
B-IS2	2.01	28.24	800	6.88
B-IS3	2.39	34.26	850	10.29
B-IS4	2.49	33.98	900	10.75
B-IS5	2.52	35.77	950	11.01
B-IS6	2.52	37.94	1000	9.77
B-IS7	2.50	31.89	1100	11.23
B-SO1	2.29	41.71	700	0.91
B-SO2	2.51	45.01	800	1.05
B-SO3	2.27	38.48	850	1.23
B-SO4	2.51	44.22	900	1.19
B-SO5	3.69	41.19	950	1.94
B-SO6	2.57	40.89	1000	3.03
B-SO7	2.56	27.74	1100	7.52
C1	2.27	9.90	1200	48.0
C2	2.33	6.50	1230	49.0
C3	2.34	7.50	1250	61.0

C4	2.33	4.70	1260	61.0
C5	2.34	4.80	1270	61.0
C6	2.33	4.00	1280	57.0
C7	2.28	8.50	1300	65.0
D1	2.24	11.64	1210	59.23
D2	2.25	10.51	1210	61.81
D3	2.26	9.67	1210	62.46
D4	2.26	9.57	1220	63.32
D5	2.26	9.37	1220	63.49
D6	2.25	8.97	1220	63.51
D7	2.20	11.58	1230	60.89
D8	2.19	11.94	1230	58.45
D9	2.16	13.86	1230	55.70

Table 2. Geometrical characteristics of the IFU model for the systems *B-IS6*, *B-IS7*, *B-SO6* and *B-SO7*. Fractal dimension D_f, maximum ray R_{max}, minimum ray R_{min}, iteration number, number of *solid forever* squares, *filled surface* and porosity *p*.

		B-IS6	B-IS7	B-SO6	B-SO7
1 Unit α	D_f	1.89	1.89	1.77	1.89
	n_α	1	1	1	1
	R_{max} (µm)	129.6	162	105	124
	Iteration	9	8	9	9
	R_{min} (µm)	0.006	0.025	0.005	0.006
	Solid forever	2	2	0	1
n Unit β	D_f	1.77	1.63	1.89	1.89
	n_β	59233	30530	3911	1622
	R_{max} (µm)	0.6	2	3.89	4.59
	Iteration	5	4	6	6
	R_{min} (µm)	0.006	0.025	0.005	0.006
	Solid forever	3	4	2	4
	Filled Surface (µm^2)	$1.69 \cdot 10^5$	$1.53 \cdot 10^6$	0	$1.67 \cdot 10^4$
	p_{exp} / p_{IFU} (%)	38	32	41	28

Table 3. Geometrical characteristics of the IFU model for the systems *M1*, *M2*, *F1*, *F2* and *F3*. Fractal dimension D_f, maximum ray R_{max}, minimum ray R_{min}, iteration number, number of *solid forever* squares, *filled surface* and porosity p.

		M1	M2	F1	F2	F3
1 Unit α	D_f	1.77	1.89	1.77	1.77	1.77
	n_α	1	1	1	1	1
	R_{max} (µm)	92	270	35	48	69
	Iteration	10	10	9	9	9
	R_{min} (µm)	0.002	0.005	0.002	0.002	0.004
	Solid forever	0	2	0	0	0
n Unit β	D_f	1.77	1.626	1.77	1.77	1.77
	n_β	$2.72 \cdot 10^7$	$5.54 \cdot 10^6$	$2.07 \cdot 10^7$	$1.74 \cdot 10^8$	$2.41 \cdot 10^7$
	R_{max} (µm)	0.042	0.123	0.016	0.022	0.003
	Iteration	3	3	2	1	2
	R_{min} (µm)	0.002	0.005	0.002	0.002	0.004
	Solid forever	4	2	4	4	4
	Filled Surface (µm^2)	$1.78 \cdot 10^6$	$1.50 \cdot 10^4$	$1.17 \cdot 10^6$	$1.20 \cdot 10^7$	$1.78 \cdot 10^6$
	p_{exp} / p_{IFU} (%)	22	53	7	10	15

Table 4. Geometrical characteristics of the IFU model for the systems *F4*, *F5*, *F6*, *F7* and *F8*. Fractal dimension D_f, maximum ray R_{max}, minimum ray R_{min}, iteration number, number of s*olid forever* squares, *filled surface* and porosity p.

		F4	F5	F6	F7	F8
1 Unit α	D_f	1.63	1.63	1.63	1.89	1.89
	n_α	1	1	1	1	1
	R_{max} (μm)	124	147	170	196	270
	Iteration	10	10	10	10	10
	R_{min} (μm)	0.002	0.002	0.003	0.003	0.005
	Solid forever	0	3	3	3	2
n Unit β	D_f	1.89	1.77	1.77	1.46	1.26
	n_β	$4.42 \cdot 10^7$	$1.80 \cdot 10^7$	$1.52 \cdot 10^7$	$5.57 \cdot 10^6$	$5.54 \cdot 10^6$
	R_{max} (μm)	0.057	0.067	0.078	0.090	0.123
	Iteration	3	3	3	3	3
	R_{min} (μm)	0.002	0.002	0.003	0.003	0.005
	Solid forever	4	4	4	3	2
	Filled Surface (μm^2)	0	$1.56 \cdot 10^6$	0	$6.39 \cdot 10^3$	$3.33 \cdot 10^4$
	p_{exp} / p_{IFU} (%)	27	32	37	42	52